



COUPLING OF RC WALLS USING UNBONDED POST-TENSIONING: APPLICATIONS IN HYBRID CONSTRUCTION

Yahya KURAMA¹, Qiang SHEN², and Brad WELDON²

SUMMARY

This paper describes an experimental program to investigate the nonlinear behavior of coupling beam subassemblages in a new type of hybrid coupled wall system. Coupling of concrete walls is achieved by post-tensioning steel beams to the walls using unbonded post-tensioning tendons, without embedding the beams into the walls. Top and seat angles are used at the beam ends to yield and dissipate energy. The results demonstrate excellent stiffness, strength, and ductility characteristics of the test specimens under cyclic loading, with considerable energy dissipation concentrated in the angles and self-centering due to post-tensioning. The specimens were able to sustain large nonlinear displacements with little damage in the beams and the wall regions. The experimental results are used to revise a previous analytical model.

INTRODUCTION

The lateral stiffness and strength of concrete structural walls can be significantly increased by coupling two or more walls using monolithic cast-in-place reinforced concrete or embedded steel beams (e.g., Harries et al. [1]). As an alternative, recent research (Shen and Kurama [2]; Kurama and Shen [3]) has shown that the use of unbonded post-tensioned steel beams may be a viable method for coupling, without embedding the beams into the walls. This paper provides an experimental evaluation of this new system and verification of a previous analytical model. The research, which was conducted as a part of the *U.S.-Japan Cooperative Earthquake Research Program on Composite and Hybrid Structures* funded by the National Science Foundation, is described in full detail in Shen et al. [4].

As an example, Fig. 1(a) shows an eight-story unbonded post-tensioned hybrid coupled walls system and Fig. 1(b) shows a wall subassemblage at a floor level. The post-tensioning (PT) force is provided by unbonded multi-strand tendons that are anchored to the walls only at the ends. The beam-to-wall interface regions include top and seat angles connected to the beam flanges and to the walls.

Fig. 1(c) shows the expected deformed shape of the subassemblage under lateral loads acting on the walls from left. The nonlinear subassemblage deformations occur primarily as a result of gap opening at the

¹ Associate Professor, Civil Engineering and Geological Sciences, University of Notre Dame, Notre Dame, Indiana, 46556 USA.

² Graduate Research Assistant, Civil Engineering and Geological Sciences, University of Notre Dame, Notre Dame, Indiana, 46556 USA.

beam-to-wall interfaces. Fig. 1(d) shows the coupling forces from a diagonal compression strut in the beam due to post-tensioning. In a properly designed subassembly, the desired behavior is yielding of the angles, with little yielding and damage in the beam and walls. The purpose of the angles is to provide energy dissipation during an earthquake. The angles also provide a part of the moment resistance of the subassembly, prevent sliding of the beam at the beam-to-wall interfaces (together with friction resistance against sliding), and serve as beam supports during construction. The yielded angles can be replaced after the earthquake.

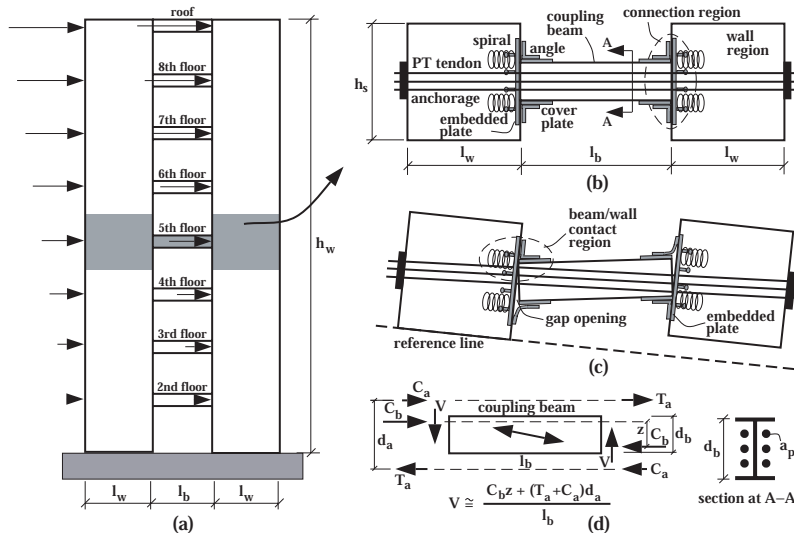


Fig. 1. Coupled wall system (adapted from Shen and Kurama [2]): (a) multistory wall; (b) subassembly; (c) deformed shape; and (d) coupling forces

The experimental program includes eleven specimens (Tests 1-11) as shown in Table 1. Only the results from Tests 1, 2, 3, and 5 are described in this paper. Results from the other tests can be found in Shen et al. [4] and Kurama et al. [5]. Test 3 was designed to represent a half-scale model of the prototype subassembly in Shen and Kurama [2].

EXPERIMENTAL PROGRAM

The experimental program includes

eleven specimens (Tests 1-11) as shown in Table 1. Only the results from Tests 1, 2, 3, and 5 are described in this paper. Results from the other tests can be found in Shen et al. [4] and Kurama et al. [5]. Test 3 was designed to represent a half-scale model of the prototype subassembly in Shen and Kurama [2].

Table 1. Test Specimens

Test	Loading	^a Beam	Cover plate (mm)	^b Angle no. & size	^c l_{gv} (mm)	Σa_p (mm ²)	^d $P_i / (\Sigma a_p f_{pu})$	^e f_{bi} / f_{by}	Test parameter
1	Cyclic	W10x68	203x124x19.1	-	95.3	560	0.55	0.099	No angles
2	Cyclic	W10x68	203x124x19.1	-	95.3	560	0.54	0.098	Retest beam
3	Cyclic	W10x68	203x124x19.1	Four L8x4x1/2	95.3	560	0.52	0.094	Base test
4	Monotonic	W10x68	203x124x19.1	Two L8x4x1/2	95.3	-	-	-	Angle test
5	Cyclic	W10x68	-	Four L8x4x1/2	114	560	0.53	0.17	No cover plates
6	Monotonic	W10x68	-	Two L8x4x1/2	114	-	-	-	Angle test
7	Cyclic	W10x68	-	Four L8x4x5/8	114	560	0.56	0.17	Thicker angles
8	Monotonic	W10x68	-	Two L8x4x5/8	114	-	-	-	Angle test
9	Cyclic	W10x68	-	Four L8x4x5/8	114	840	0.55	0.25	Larger PT area
10	Cyclic	W14x99	-	Four L8x4x5/8	138	560	0.52	0.16	Larger beam depth
11	Cyclic	W14x99	-	Four L8x4x5/8	138	-	-	-	Angle test

^aU.S. shape. The beam flanges were saw-cut to a width of 159 mm. ^bU.S. shape.

^cAngle vertical leg gage length measured from the center of the innermost angle-to-wall connectors to the heel of the angle.

^d P_i =total initial force measured in the beam PT strands; f_{pu} =design ultimate strength for the strands (1862 MPa).

^e f_{bi} =total beam initial PT force divided by gross cross section area (including cover plates); f_{by} = beam yield strength (386 MPa).

Test Set-Up

Fig. 2(a) shows the elevation view of the half-scale experimental set-up, which includes two reinforced concrete wall regions placed at each end of a steel coupling beam. The left wall region, referred to as the “reaction block”, is fixed to the strong floor. The right wall region, referred to as the “loading block”, is connected to two actuators hanging from a steel loading frame. The actuators are used in displacement control to move the loading block up or down without rotating it; thus, modeling the deformed configuration in Fig. 1(c). The loading block is free to move in the horizontal direction. An inner steel frame (not shown) is used to prevent out-of-plane movement of the loading block at three points, and of the coupling beam at the midspan.

Loading Block and Reaction Block

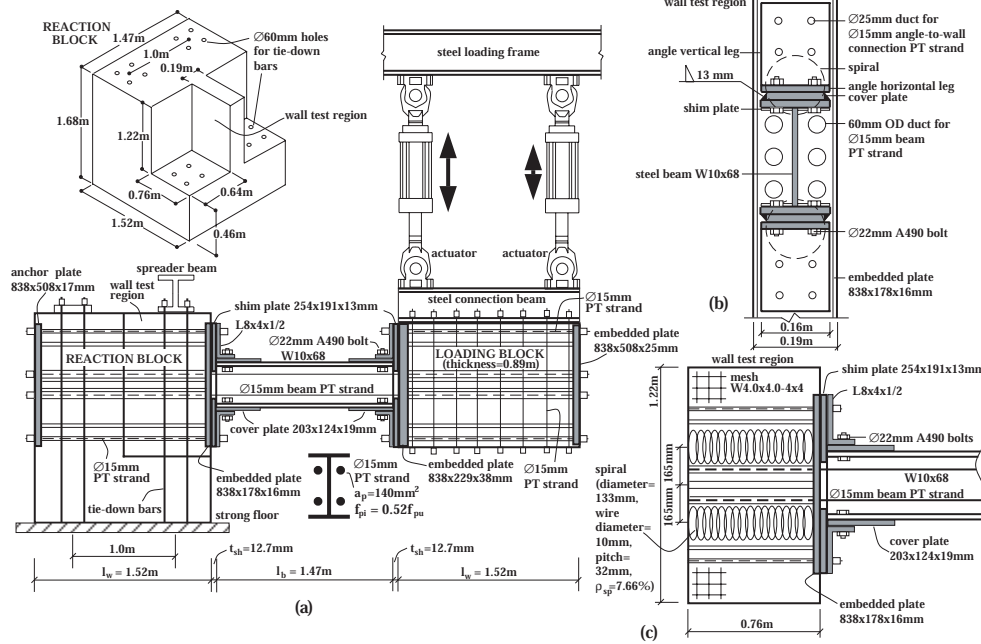


Fig. 2. Test set-up: (a) elevation; (b) beam end view; and (c) beam-to-wall connection region

does not have a uniform thickness [Fig. 2(a)]. Adjacent to the coupling beam, the width of the reaction block is 191 mm, modeling the thickness of the prototype wall. This region of the block is referred to as the wall test region. Note that half-scale similitude requires a wall thickness of $t_w=178$ mm; however, a slightly larger thickness was necessary to accommodate the use of oversized PT ducts in the block with adequate concrete cover and reinforcement. The other regions of the reaction block are 1.47 m wide to provide lateral stability to the block and to allow tie-down to the strong floor.

Coupling Beams

Steel U.S. wide-flange shapes (Table 1) are used for the coupling beams, with length equal to $l_b \cong 1.47$ m (one half the full-scale prototype beam length). In order to satisfy half-scale similitude requirements with the W21x182 prototype beam, the flanges of the test beams were saw-cut to a width of $b_f=159$ mm (one half the full-scale flange width). Fig. 2(b) shows the beam-end-view of the test set up.

Post-Tensioning Strands

Seven-wire strands (with 15.2 mm nominal diameter) are used to apply the PT force. Six test specimens had two pairs of strands (placed on either side of the beam web), one specimen had three pairs of strands, and four specimens had no PT strands. The resulting total PT steel areas, Σa_p , are given in Table 1. Note that the steel area required for similitude with the prototype beam is equal to 630 mm^2 , which is slightly larger than the area provided in Test 3. Each PT strand is run through oversized ducts inside the reaction and loading blocks, and is anchored to the far ends of the blocks using a steel wedge/barrel anchorage system. The strands are not bonded to the blocks or connected to the beam between the anchors.

Beam-to-Wall Connection Regions

The beam-to-wall connection regions [Fig. 2(c)] include embedded steel plates, wire mesh reinforcement, and spiral reinforcement inside the loading and reaction blocks; and flange cover plates (in Tests 1-4; see Table 1), shim plates, and top and seat angles at the beam ends as described in more detail below.

The lengths of the loading and reaction blocks are equal to $l_w=1.52$ m (one half the length of the full-scale prototype wall in Shen and Kurama [2]). The loading block [Fig. 2(a)] has a uniform width (thickness) of 889 mm along its length in order to accommodate the connections to the two actuators and to prevent damage to the block during testing.

The reaction block

Embedded Plates – Embedded steel plates, placed flush with the outside of the reaction and loading blocks during casting (with nominal welded studs) are used to distribute the compressive stresses in the concrete in the contact regions near the beam-to-wall interfaces [Figs. 2(a) and 2(c)]. The embedded plate inside the reaction block has a thickness of $t_c=16.0$ mm (one half the embedded plate thickness in the full-scale prototype wall) and a width of 178 mm. A thicker 38 mm plate is used in the loading block to prevent damage to the block during testing.

Spiral Reinforcement – Two spirals are used behind the embedded plates in each of the reaction and loading blocks, one spiral near each coupling beam flange as shown in Figs. 2(b) and 2(c). The spiral wire diameter is 10 mm, spiral diameter is 133 mm, and spiral pitch is 32 mm. The length of the spiral is 889 mm inside the reaction block and 305 mm inside the loading block. In addition to the spirals, W4.0xW4.0-4x4 welded wire mesh (with 5.7 mm wire diameter) is used on both faces of the 191-mm thick wall test region of the reaction block.

Flange Cover Plates – Beam flange cover plates with a thickness of $t_c=19.1$ mm, width of 124 mm, and length of $l_c=203$ mm (one half the full-scale cover plate length) are used in Tests 1-4 to minimize the yielding and deformations of the coupling beam flanges in compression. As shown in Fig. 2(b), the cover plates are placed flush with the beam ends and are fillet welded to the top and bottom flanges.

Shim Plates – Shim plates are used between the coupling beam flanges and the embedded plates in the reaction and loading blocks. The shim plates are welded to the embedded plates and are terminated at the beam web [Fig. 2(c)], thus preventing contact between the web and the concrete blocks. This is done to force the bearing between the coupling beam and the walls to occur at the flanges, so that one or both flanges remain in contact with each block during the cyclic displacements of the subassembly. The shim plates in the test specimens have a thickness of $t_{sh}=12.7$ mm, width of 191 mm, and length of 254 mm. In practical applications, shim plates may also be used for construction tolerances.

Top and Seat Angles – The top and seat angles in Tests 3-6 have L8x4x1/2 cross sections and the angles in Tests 7-11 have L8x4x5/8 cross sections. The angle length is equal to the beam flange width of $b_f=159$ mm. As shown in Fig. 2(c), the angles are oriented such that the shorter leg is parallel to the beam flange and is bolted to the beam flange using two A490 $\text{Ø}22.2$ mm (Tests 3-9) or $\text{Ø}25.4$ mm (Tests 10, 11) slip critical bolts installed using the “turn-of-nut pretensioning method” (AISC [6]). The connection between the vertical leg of each angle and the reaction block or the loading block is achieved using two or four 15.2 mm diameter seven-wire unbonded PT strands, each prestressed to approximately $f_{pi}=0.50f_{pu}$, where $f_{pu}=1862$ MPa is the design ultimate strength of the PT steel. The connection gage lengths, l_{gv} for the vertical legs of the angles in the experiments are given in Table 1. The purpose of the longer angle vertical legs is to allow for parameter variations in the angle gage length, l_{gv} .

Each PT strand in an angle-to-wall connection is passed through a 25.4 mm diameter duct and is unbonded along its entire length (i.e., the length of the concrete block) to prevent yielding as the angles are pulled by the beam during the experiments. Each strand is anchored at the far end of the concrete block, thus putting the concrete into compression. Note that it may also be possible to use bolted or welded angle-to-wall connections. These connection types were not used in this research to prevent the development of large tensile stresses in the concrete. Furthermore, yielding and fracture of the angle-to-wall bolts may be possible, thus reducing the ductility of the connection and preventing the angles from yielding and dissipating energy effectively.

Loading

Two 978.6-kN hydraulic actuators [Fig. 2(a)] were used in displacement control to move the loading block up and down through the cyclic displacement history in Fig. 3(a). In order to restrain the loading

block from rotating in the vertical plane (i.e., the plane of the test set-up), the actuators were moved by the same displacement, resulting in actuator forces in opposite direction. A two-channel Schenck Pegasus 5910 Digital Controller and a computer were used to send the displacement command signal to the two actuators simultaneously to prevent significant lag between the actuators.

Table 1 shows the total initial (after short-term losses) forces measured in the beam PT strands, P_i normalized with the design ultimate strength $\Sigma a_p f_{pu}$. Each PT strand was prestressed using a mono-strand hydraulic jack. A considerable amount of prestress was lost at the anchors during post-tensioning, which

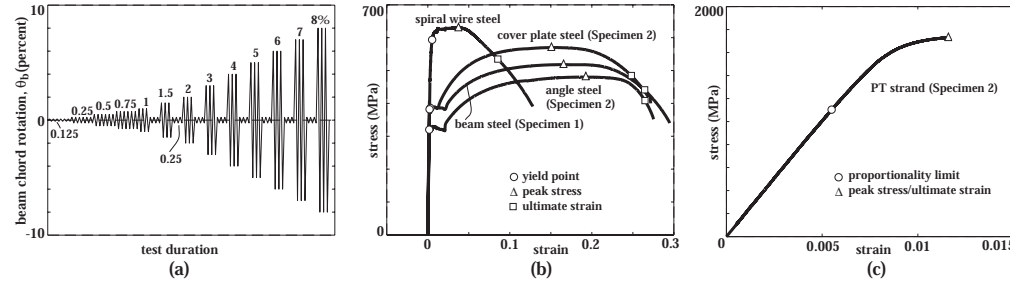


Fig. 3. Test information: (a) displacement history; (b) beam, cover plate, angle, spiral wire steel; and (c) PT strand

resulted in smaller initial stresses in the strands than the design initial stress of $0.60f_{pu}$ in the prototype subassembly.

Eight 25.4 mm diameter tie-down steel bars [Fig. 2(a)] were used to apply a nominal compression (i.e., downward) axial force of 1379 kN to the 191-mm thick wall test region of the reaction block (adjacent to the coupling beam). This axial force was kept relatively constant during each test.

Material Properties

ASTM (American Society for Testing and Materials) standards were followed to determine the properties of the beam steel, cover plate steel, angle steel, spiral steel, PT strand (ASTM 370), and the wall concrete (ASTM C39/C 39M). Figs. 3(b) and 3(c) show typical measured stress-strain relationships for the beam, cover plate, angle, spiral, and strand materials. Steel wedge/barrel type PT anchors were used to pull the strands until failure, to provide anchor conditions similar to those in the subassembly experiments. The strand specimens were approximately 1.22 m long (between anchors) and were carefully positioned between the machine heads for proper alignment. Failure of all strand specimens occurred due to the fracture of a PT wire at an anchor, at an average stress of $f_{pu}=1698$ MPa, well below the design ultimate strength of $f_{pu}=1862$ MPa. Selected results from the steel and concrete material tests can be found in Table 2. The yield stress and strain for the spiral steel were determined assuming a 0.2% strain off-set at zero stress upon unloading from the yield point using the measured Young's modulus.

Table 2. Material Properties

Spec. No	Beam Steel		Cover Plate Steel				Angle Steel				PT Strand				Concrete		
	f_{by} (MPa)	ϵ_{by}	f_{bu} (MPa)	ϵ_{bu}	f_{cy} (MPa)	ϵ_{cy}	f_{cu} (MPa)	ϵ_{cu}	f_{ay} (MPa)	ϵ_{ay}	f_{au} (MPa)	ϵ_{au}	f_{py} (MPa)	ϵ_{py}	f_{pu} (MPa)	ϵ_{pu}	f'_c (MPa)
1	390	0.0019	519	0.265	399	0.0019	572	0.269	334	0.0019	486	0.198	1138	0.0056	1696	0.0098	66.8
2	386	0.0018	531	0.300	380	0.0020	570	0.248	321	0.0016	487	0.267	1103	0.0055	1724	0.0098	48.3
3	383	0.0020	521	0.281	383	0.0017	573	0.212	327	0.0017	483	0.288	1069	0.0053	1674	0.0116	67.6

Notes: 1. f_{by} , f_{cy} , f_{ay} =lower yield stress; ϵ_{by} , ϵ_{cy} , ϵ_{ay} = f_{by} , f_{cy} , or f_{ay} divided by measured Young's modulus [\circ markers in Fig. 3(b)]; f_{bu} , f_{cu} , f_{au} =peak stress [Δ markers in Fig. 3(b)]; ϵ_{bu} , ϵ_{cu} , ϵ_{au} =ultimate strain at $0.85f_{bu}$, $0.85f_{cu}$, or $0.85f_{au}$ [\square markers in Fig. 3(b)]. 2. f_{py} =limit of proportionality; ϵ_{py} = f_{py} divided by measured Young's modulus [\circ marker in Fig. 3(c)]; f_{pu} =peak stress; ϵ_{pu} =ultimate strain at f_{pu} [Δ marker in Fig. 3(c)]. 3. f'_c =peak stress of unconfined reaction block concrete.

Instrumentation

The test instrumentation includes the following (Fig. 4):

Load cells – (1) two load cells (LC1 and LC2) to measure the actuator forces; (2) up to six load cells (LC3-LC8) to measure the forces in the beam PT strands; (3) two load cells (LC9-LC10) to measure the

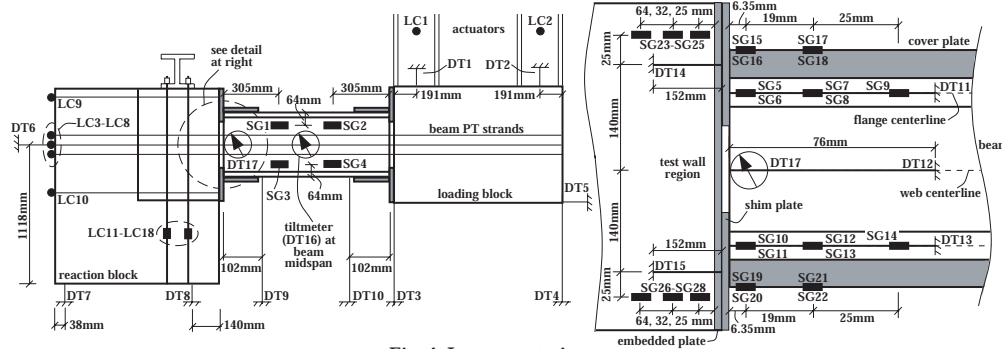


Fig. 4. Instrumentation

forces in the angle-to-wall connection PT strands; and (4) eight load cells (LC11-LC18) to measure the vertical forces applied to the wall test region of the reaction block.

Displacement/rotation transducers in the vertical plane – (1) two displacement transducers (DT1 and DT2) to measure the actuator displacements; (2) three transducers (DT3-DT5) to measure the loading block displacements; (3) three transducers (DT6-DT8) to measure the reaction block displacements; (4) two transducers (DT9 and DT10) to measure the coupling beam displacements; (5) three transducers (DT11-DT13) to measure the gap opening displacements between the coupling beam and the reaction block; (6) two displacement transducers (DT14 and DT15) to measure the local horizontal deformations of the reaction block in the wall test region; and (7) two tiltmeters (DT16-DT17) to measure the coupling beam rotations at the midspan and at the reaction block end.

Electrical resistance strain gages – (1) four strain gages (SG1-SG4) to measure the horizontal strains of the coupling beam web along the length; (2) up to eighteen gages (SG5-SG22) to measure the horizontal strains in the coupling beam flanges and cover plates near the reaction block; and (3) six gages (SG23-SG28) to measure the internal strains in the wall test region of the reaction block. Strain gages SG23-SG28 were attached to horizontal #3 deformed bars tied to the spiral reinforcement inside the concrete.

Test Procedure

Each subassembly was subjected to the following test procedure: (1) determine the forces in the actuators due to the self weight of the subassembly; (2) apply the initial stresses to the beam PT strands; (3) use the actuators in load control to counteract the self-weight forces from Step 1; (4) connect the top and seat angles to the beam and to the reaction and loading blocks; and (5) use the actuators in displacement control to apply the loading history in Fig. 3(a).

RESULTS OF EXPERIMENTS

The results from Tests 1, 2, 3 and 5 are evaluated below. In Test 1, top and seat angles were not used at the beam-to-wall connections to study the behavior of the subassembly and to verify the analytical models without the angles. In Test 2, the coupling beam used in the first test was retested after replacing and re-stressing the PT strands. In Test 3, a new beam with top and seat angles at the beam-to-wall connections was used, representing the prototype subassembly described in Shen and Kurama [2]. In Test 5, a beam with no flange cover plates was investigated.

Test 1

Fig. 5(a) shows the coupling shear force versus rotation ($V_b-\theta_b$) behavior from Test 1. The force V_b is determined from the actuator forces and the rotation θ_b is the coupling beam chord rotation determined from transducers DT9 and DT10. Only the first cycle during each set of displacement cycles of equal amplitude is shown, except where significant differences occur in the second and/or third cycles. The hysteresis loops in Fig. 5(a) demonstrate that the behavior of the subassembly without angles is essentially bilinear-elastic, caused mainly by gap opening at the beam-to-wall interfaces. A small amount

of reduction in prestress initiated at about $\theta_b=2\%$ (due to nonlinear behavior in the strands and/or anchorages), resulting in a small reduction in V_b during subsequent displacement cycles of increasing amplitude. The reduction in prestress did not cause a reduction in the strength of the specimen. Failure of the subassembly occurred when one of the seven wires in a PT strand fractured at the end of the second cycle to $\theta_b=-8\%$ in the negative (i.e., counter clockwise) direction. The fracture occurred inside a PT anchor (similar to the failure mode observed in the material tests) at a premature stress of 1466 MPa (well below the average peak stress of $f_{pu}=1698$ MPa from the material tests), and resulted in a small reduction in V_b . The maximum PT stress reached during the test was 1576 MPa. The subassembly was unloaded and the experiment was terminated. No damage was observed in the reaction block or the loading block during the test, allowing both blocks to be reused in all of the subsequent tests.

Test 2

The coupling beam used in the first test did not receive any significant damage other than a small amount of compression yielding in the cover plates at the very ends. To demonstrate this, the beam was retested after replacing and re-stressing the PT strands. Note that only selected displacement cycles from Fig. 3(a) were used in this second test. The behavior of the retested beam in Fig. 5(b) is very similar to the behavior of the original beam in Fig. 5(a); with small differences since all or most of the yielding in the beam cover plates occurred in Test 1. The results demonstrate that unbonded post-tensioned hybrid coupled wall subassemblies can go through large nonlinear displacements without receiving significant damage in the walls or the beams. The beams do not need to be replaced after a large earthquake as long

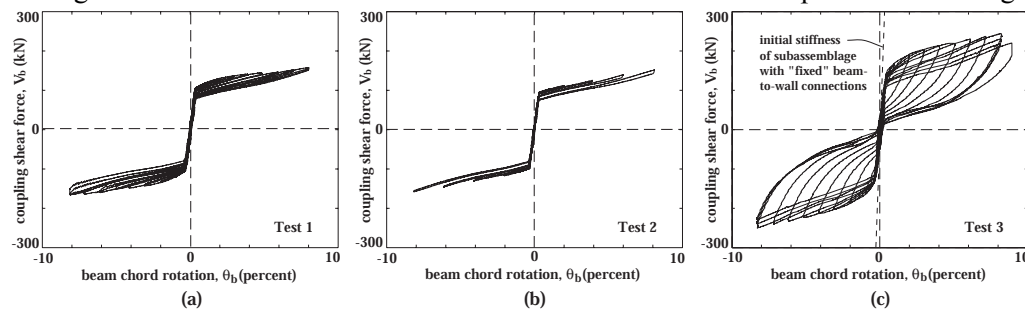


Fig. 5. Measured coupling beam rotation versus shear force relationships: (a) Test 1; (b) Test 2; and (c) Test 3

as the damaged, yielded, or fractured strands are replaced and re-stressed. Figs. 5(a) and 5(b) show that there is a small increase in the post-softening stiffness of the subassembly after about $\theta_b=4\%$ rotation. This occurred as a result of “kinking” of the strands due to contact with the oversized PT ducts at the beam-to-wall interfaces, leading to increased P- Δ effects in the strands. Kinking of the PT strands did not have any undesirable effects on the behavior of the subassemblies. Note that the fracture of the strand in Test 1 occurred inside an anchor and not along the length of the strand. The PT strands in Test 2 did not fracture, and the test was terminated after unloading from the third cycle to $\theta_b=8\%$ rotation, without failure.

Test 3

Fig. 5(c) shows the V_b - θ_b behavior of the subassembly with top and seat angles from Test 3. As described earlier, this specimen is a half-scale model of the prototype subassembly described in Shen and Kurama [2]. The hysteresis loops indicate desirable seismic characteristics with stable behavior up to $\theta_b=8\%$ rotation and significant energy dissipation. Comparing Figs. 5(a) and 5(c), the increase in the energy dissipation occurs as a result of yielding of the angles.

Fig. 6(a) shows the overall displaced shape of Test 3 at $\theta_b=+8\%$ rotation in the positive (i.e., clockwise) direction and Fig. 6(b) shows a close-up view of the test region near the reaction block at $+8\%$ rotation. The displaced shape of the subassembly is similar to the displaced shape in Fig. 1(c), with most of the beam rotation occurring as a result of the gaps at the beam ends. The rotation of the beam results in the yielding of the top and seat angles in tension and compression as shown in Figs. 6(a) and 6(b).

The straight dashed line in Fig. 5(c) shows the theoretical initial (i.e., linear-elastic) stiffness of the same subassembly assuming fixed beam-to-wall connections (representing an embedded beam). As a result of post-tensioning, the measured initial stiffness of the test beam before the initiation of gap opening is similar to the initial stiffness of the fixed beam. The hysteresis loops in Fig. 5(c) indicate that the PT strands provide a large enough restoring force such that the gaps are closed upon unloading, thus pulling the beam towards its undeformed position with little residual displacement (i.e., self-centering capability). The initial stiffness of the structure is preserved even after unloading from very large nonlinear rotations.

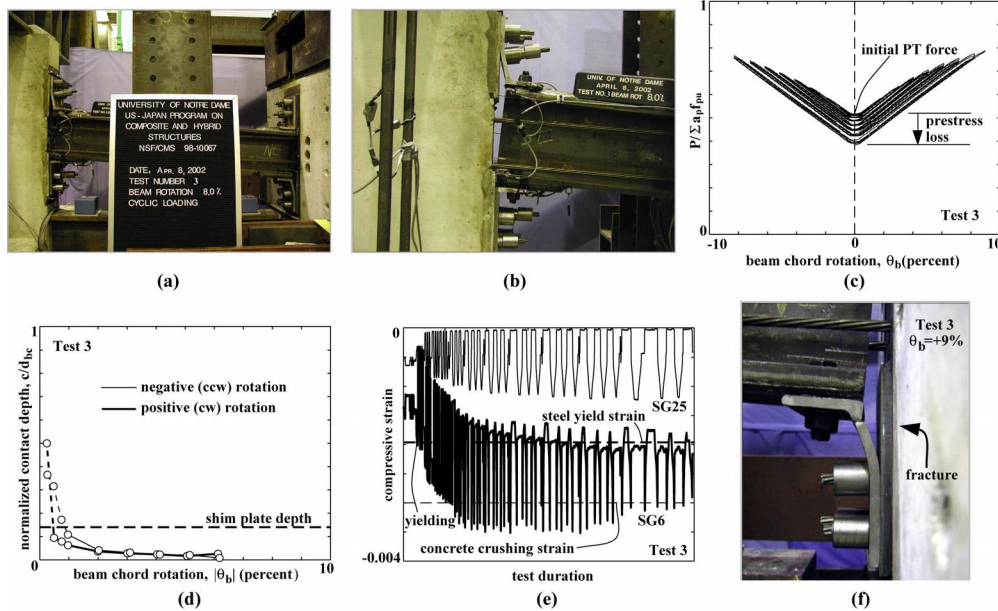


Fig. 6. Test 3: (a) displaced shape-overall; (b) displaced shape-local; (c) total PT force; (d) contact depth; (e) flange steel and wall concrete strains; and (f) angle fracture

resisting gap opening. There is a small loss in the total beam PT force upon unloading to zero displacement, indicating nonlinear behavior in the strands and/or anchorages. Unlike Test 1, fracture of the PT strands did not occur in Test 3.

Fig. 6(d) shows the depth of contact, c between the coupling beam and the reaction block in Test 3, as determined from displacement transducers DT11-DT13 at the beam end. The contact depth is normalized with respect to the depth of the beam including the cover plates, $d_{bc}=302$ mm. Each circular marker represents the measured contact depth upon first loading to a peak θ_b value in the positive or negative direction during the displacement history followed in the test. Under small rotations of the beam, the entire beam depth is in “contact” with the reaction block (note that the beam depth between the shim plates is not in contact). The initiation of gap opening (i.e., decompression) occurs before $\theta_b=0.25\%$ and results in a rapid reduction of the contact depth. Values of c below the horizontal dashed line indicate that the contact depth is within the shim plate. A contact depth of $c=12.5$ mm (approximately 0.66 times the cover plate thickness, t_c) is reached at $\theta_b=2\%$, beyond which the contact depth changes relatively little.

To investigate the amount of yielding in the beam flanges in Test 3, the deformations were measured using strain gages SG5-SG14 located at the flange centerline. As an example, the thick solid line in Fig. 6(e) shows the top flange strains in SG6 (see Fig. 4). Application of the PT force results in a compressive strain at the beginning of the test. The strain readings cycle but remain compressive (due to gap opening) as the beam is rotated in the positive and negative directions. As a result of gap opening, the compression strain in SG6 drops to a minimum value during the first cycle to $\theta_b=+0.25\%$. Upon loading in the reversed direction to $\theta_b=-0.25\%$, the strain in SG6 reaches the measured average (from three specimens) yield strain of $\epsilon_{by}=-0.0019$ (indicated by the thick dashed horizontal line). As shown in Fig. 6(e), there is an

The sum of the coupling beam PT forces, P in Test 3 (normalized with respect to the total design ultimate strength of the PT steel, $\Sigma a_p f_{pu}$) is plotted in Fig. 6(c). Before the initiation of gap opening, the forces in the PT strands are similar to the initial PT forces. As the specimen is displaced further, the strand forces increase, thus

accumulation of plastic (i.e., residual) compressive strains in the beam flange upon unloading from θ_b values beyond 0.25%. The maximum strain measured in SG6 is -0.0035 (approximately equal to $1.8\epsilon_{by}$). It is concluded that the amount of yielding in the flanges of the beam in Test 3 was negligible.

Similarly, in order to investigate the performance of the reaction block, the deformations in the 191-mm thick wall test region were measured using DT14-DT15 and SG23-SG26 (see Fig. 4). As an example, the thin solid line in Fig. 6(e) shows the strains from SG25, which remain compressive during the test. The thin dashed horizontal line corresponds to the assumed unconfined concrete spalling/crushing strain of -0.003. It is concluded that the wall test region did not receive any damage during the test, including cracking and/or spalling of the cover concrete [see Fig. 6(b)].

Initiation of low cycle fatigue cracks was observed in the vertical legs of the tension angles at about $\theta_b=7\%$. The cracks occurred at the critical section adjacent to the fillet. The subassembly was able to sustain three displacement cycles at $\theta_b=8\%$ with a steady, but not excessively large, reduction in strength and stiffness as shown in Fig. 5(c). This reduction in stiffness and strength occurred due to increased cracking and necking of the vertical legs of the tension angles. Failure of the subassembly eventually occurred as a result of the complete fracture of the vertical leg of the bottom angle at the right end of the beam when $\theta_b=+9\%$ was reached for the first time. The resistance of the specimen at this stage was, approximately, 90% of the peak resistance. Fig. 6(f) shows the fractured angle at $\theta_b=+9\%$. All four angles sustained significant damage resulting in a considerable amount of energy dissipation as shown in Fig. 5(c). The subassembly was unloaded and the test was terminated upon fracture of the first angle.

As shown in Fig. 6(b), the angle-to-wall connections performed extremely well, allowing the angles to go through large nonlinear deformations without damaging the concrete. The integrity of the angle-to-wall connections was preserved during the entire test since the connection strands did not yield. The angle-to-beam connections also behaved satisfactorily, with no slip between the beam and the angles up to $\theta_b=5\%$ and negligible slip afterwards, indicating that the slip-critical bolts were adequate. Slip between the coupling beam and the reaction and loading blocks did not occur indicating that the angles provided adequate vertical support to the beam together with friction resistance due to post-tensioning.

Test 5

A coupling beam with no flange cover plates was used in Test 5 to determine the effectiveness of the cover plates in strengthening and stabilizing the flanges. As a second difference, the gage length l_{gv} for the angle vertical legs in Test 5 was longer than the gage length in Test 3 by an amount equal to the cover plate thickness of $t_c=19.1$ mm (Table 1). The measured $V_b-\theta_b$ behavior from Test 5, shown in Fig. 7(a), illustrates the stable behavior of the subassembly. Failure of the subassembly occurred as a result of the complete fracture of the vertical leg of the top angle at the right end of the beam when $\theta_b=-7\%$ was

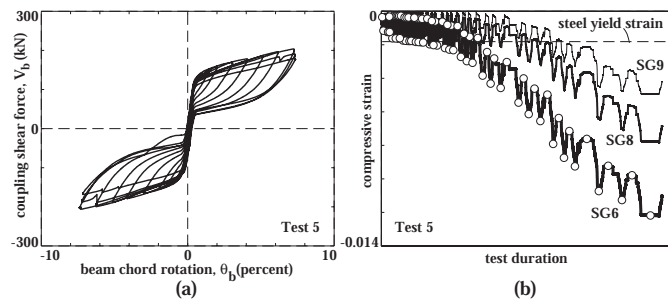


Fig. 7. Test 5: (a) $V_b-\theta_b$ relationship; and (b) flange strains

reached for the third time, after which the subassembly was unloaded and the test was terminated. The angle-to-beam and angle-to-wall connections performed as desired, with no slip or failure during the entire test.

As compared with Test 3 [Fig. 5(c)], the peak coupling shear resistance and energy dissipation from Test 5 [Fig. 7(a)] are smaller.

This is possibly due to the increase in the angle gage length, which led to a reduction in the angle contribution to the coupling shear force. Two monotonic tests (Tests 4 and 6) with only two tension angles and no beam PT steel were conducted to get more information on the angle behavior as described in Shen et al. [4] and Kurama et al. [5].

In order to investigate the nonlinear behavior of the coupling beam from Test 5, Fig. 7(b) shows the flange strains at the top left end of the beam (from strain gages SG6, SG8 and SG9 located at the flange centerline, see Fig. 4). The strain readings remain compressive [similar to Fig. 6(e)] and increase under negative θ_b (i.e., when the loading block is moved upward), and decrease under positive θ_b . The circular markers show the maximum and minimum readings in strain gage SG6 corresponding to peak θ_b values in the negative and positive directions, respectively. The flange strain reaches the beam yield strain $\epsilon_{by} = -0.0019$ (indicated by the dashed horizontal line) at approximately $\theta_b = -1.5\%$, after which there is an accumulation of plastic (i.e., residual) strains upon unloading. The delayed yielding in Test 5 as compared with Test 3 could be due to uneven initial contact at the beam-to-wall interfaces. The maximum strain measured in SG6 at the beam end is -0.012 (approximately equal to $6\epsilon_{by}$). The measurements from the three gages indicate that the beam strains quickly diminish away from the beam end. It is concluded that the lack of cover plates resulted in an increase in the coupling beam flange strains [as compared with Test 3, Fig. 6(e)]; however, this did not have any adverse effects on the performance of the beam.

ANALYTICAL MODELING

Using the experimental results above, this section proposes a revised analytical model based on a model previously developed by Shen and Kurama [2]. The revised analytical model is shown in Fig. 8(a). The DRAIN-2DX Program (Prakash et al. [7]) is used as the analytical platform, with the assumptions that pertain to the model provided in Shen and Kurama [2]. Analytical models for multi-story walls are constructed by joining subassemblage models at the floor and roof levels as described in Kurama and Shen [3].

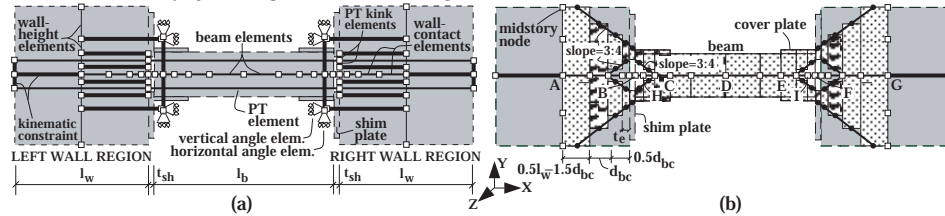


Fig. 8. Revised analytical model: (a) subassemblage; and (b) wall-contact elements and beam elements

As shown in Fig. 8(a), each concrete wall region in a coupled wall subassemblage is modeled using two sets of fiber beam-column elements. The first set consists of “wall-height elements” in the vertical direction to model the axial-flexural and shear behavior of the wall along its height. The second set is used to model the local behavior of the wall contact regions to the left and right of the coupling beam. These elements, referred to as the “wall-contact elements”, are determined from an “effective” wall cross section in the vertical Y-Z plane as described later. Truss elements are used to model the PT tendons and fiber beam-column elements are used to model the axial-flexural and shear behavior of the coupling beams. To model gap behavior, the tensile strength and stiffness of the fibers next to the beam-to-wall interfaces are set to zero (Shen and Kurama [2]). The reduction in the stiffness of the subassemblage due to gap opening is captured by the zero stiffness of the fibers that go into tension near the interfaces.

The modeling of the coupling beams and wall contact regions, the PT tendons, and the top and seat angles in the revised model are described below. The modeling of the wall height elements and gap opening/closing behavior at the beam-to-wall interfaces remain the same as the previous model.

Modeling of the Coupling Beams and Wall Contact Regions

As described in the experimental program above, shim plates are used at the beam-to-wall interfaces to prevent contact between the coupling beam web and the walls, so that one or both flanges of the beam remain in contact with each wall at any time during the cyclic displacements of the structure. The previous analytical model did not include any shim plates, allowing full contact between the beam and the walls at zero rotation. Three changes are made in the revised model to account for the shim plates [Fig. 8(b)]: (1) the thickness of the shim plates is included in the model; (2) an “effective” beam cross section is used near the beam ends instead of the full cross section; and (3) the “effective” cross section of the wall-

contact elements is revised. The dotted regions in Fig. 8(b) show the effective cross sections used in the beam and wall-contact elements in the revised model, including the shim plates. The width of the effective wall and beam cross sections are assumed to be equal to the wall thickness and beam flange/web width, respectively. The effective depth is assumed to increase away from the shim plates with a slope of 3:4. The Y-translational DOF of Node B is kinematically constrained to Node A assuming no slip occurs at the beam-to-shim-plate interface. The rotational and X-translational DOFs of Node B are not constrained. The modeling of the right wall region is similar to the left wall region.

Modeling of the Post-Tensioning Tendons

As shown in Fig. 8(a), three truss elements are used to model a PT tendon in the revised model, whereas only one truss element was used to model each tendon in the previous model. The objective of this modification is to model the kinking of the PT tendons at the beam-to-wall interfaces, which occurs when the displacement of the subassembly is large enough to cause the tendons to come into contact with the PT ducts. The truss elements representing a PT tendon are connected to each other at nodes located at the beam-to-wall interfaces. These nodes are free to move in the horizontal direction (since the PT tendons are unbonded), but are restrained from moving in the vertical direction by gap/contact PT “kink” elements above and below. Each PT kink element is connected to a second node, which is kinematically constrained to a wall-height element node at the same elevation. An initial gap is defined to model the distance between the outside of the PT tendon and the inside of the PT duct. Contact between the PT tendons and the ducts occurs when the displacement of the subassembly is large enough to close the initial gap. Once in contact, the PT kink elements prevent further vertical displacements of the truss element nodes at the beam-to-wall interfaces, modeling the kinking effect. Second order P- Δ effects should be included in the truss elements for the PT tendons to capture the increase in the coupling resistance and stiffness due to kinking as observed in the subassembly experiments.

Modeling of the Top and Seat Angles

In the previous subassembly model, the contribution of the top and seat angles to the coupling shear force was modeled using fiber elements placed parallel to the coupling beam (Shen and Kurama [2]). It was assumed that the vertical legs of the angles are loaded horizontally (i.e., parallel to the beam). Based on the experimental results, two modifications are made to this model: (1) the hysteretic model for the behavior of the angles in the horizontal direction is revised; and (2) the deformation of the horizontal legs of the angles due to the rotation of the coupling beam is included.

In the revised model, each angle is represented using two zero-length spring elements in the X- and Y-directions, respectively [Fig. 8(a)]. The moments in the angle legs are ignored. The first spring element, which represents the behavior of the angle in the horizontal (i.e., X) direction, is referred to as the “horizontal angle element”. The second element, referred to as the “vertical angle element”, represents the behavior of the angle horizontal leg due to the rotation of the coupling beam and is in the vertical (i.e., Y) direction. Both elements are connected to the same pair of nodes with identical coordinates located at the centroid of the bolt group connecting the angle horizontal leg to the beam flange and at the same elevation as the middle of the horizontal leg thickness. It is assumed that the angle-to-wall and angle-to-beam connections are properly designed for the maximum angle forces and deformations. Based on this assumption, one of the angle nodes is kinematically constrained to a wall-height element node at the same elevation and the other angle node is kinematically constrained to a corresponding beam node.

The force-deformation relationships of the horizontal and vertical angle elements are defined in the horizontal (i.e., X) and vertical (i.e., Y) directions, as shown in Figs. 9(a) and 9(b), respectively. Under tensile loading in the horizontal direction, the “yield” strength, T_{ayx} and initial stiffness, k_{aixt} are determined using a method developed by Kishi and Chen [8] and Lorenz et al. [9]. In this model, the vertical leg is assumed to be fixed along the edge of the line of angle-to-wall connectors and is pulled

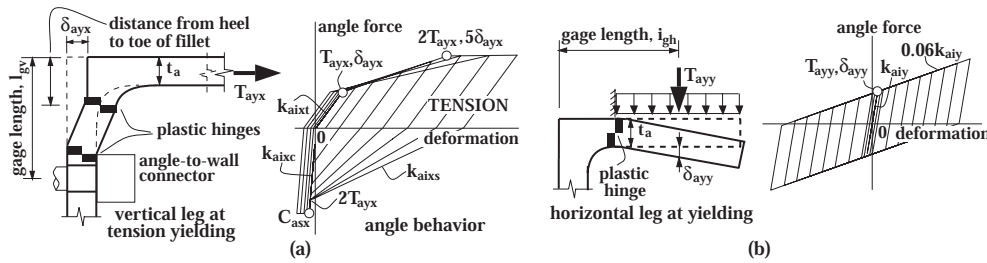


Fig. 9. Angle model: (a) horizontal angle element; and (b) vertical angle element

horizontally by the coupling beam flange like a cantilever. The yield strength, T_{ayx} is reached when the plastic collapse mechanism in Fig. 9(a) develops,

considering the interaction between the bending moment and shear in the vertical leg. The post-yield hysteretic behavior of the horizontal angle element was determined based on the subassembly experiments. It is assumed that the ultimate strength in tension is equal to 2 times the yield strength, T_{ayx} , and is reached at an angle deformation of 5 times the yield deformation, $\delta_{ayx} = T_{ayx}/k_{aixt}$. A new type of zero-length spring element was developed in DRAIN-2DX to achieve this hysteretic behavior.

Under compression, the initial stiffness of an angle as it is pushed back towards the wall by the coupling beam flange is assumed to be equal to $k_{aixc} = (1/40)E_a A_a / l_{gh}$, where E_a is the Young's modulus for the angle steel, A_a is the gross cross section area of the angle horizontal leg, and l_{gh} is the gage length of the angle horizontal leg measured from the centroid of the angle-to-beam connection bolt group to the heel of the angle. The angle unloading stiffness from a tensile deformation is assumed to be the same as the initial stiffness in tension, k_{aixt} , and the stiffness upon crossing the zero-force axis is assumed to be equal to the shooting stiffness, k_{aixs} . The angle force-deformation behavior is assumed to shoot towards the smallest of the following three forces on the initial linear-elastic loading branch in compression: (1) a compressive force with magnitude equal to the unloading force in tension; (2) the compression force reached assuming $k_{aixs} = k_{aixt}$; and (3) the "yield" strength of the angle in compression. The angle compression yield strength is assumed to be equal to the slip force, C_{asx} for the bolts connecting the angle horizontal leg to the beam flange. Note that the development of the full compression bearing capacity of the angles is not expected, and, is not modeled. In Fig. 9(a), the slip critical capacity of the angle-to-beam bolts, C_{asx} is larger than the assumed ultimate capacity of the angle in tension, $2T_{ayx}$, and thus, slip does not occur in tension.

Note also that the horizontal angle element alone represents an incomplete idealization of the behavior of the top and seat angles in a coupled wall subassembly. The model assumes that the angles are loaded horizontally, while rotations of the angle horizontal legs with respect to the vertical legs occur as the beam rotates and gaps open at the beam-to-wall interfaces. The vertical angle elements model this effect. The hysteretic load-deformation behavior of the vertical angle elements is determined using the idealized model in Fig. 9(b). It is assumed that the horizontal leg of the angle acts as a cantilever loaded uniformly in the vertical direction by the coupling beam flange. The initial stiffness, k_{aiy} and yield force, T_{ayy} are determined based on the equivalent force applied and the corresponding displacement at the centroid of the angle-to-beam connection bolt group (where the angle nodes are located in the analytical model). The plastic collapse mechanism in Fig. 9(b) is used to determine the angle yield force, T_{ayy} . The post-yield stiffness of the horizontal angle elements is assumed to be equal to 6% of the initial stiffness, k_{aiy} .

EVALUATION OF THE REVISED ANALYTICAL MODEL

This section provides a critical evaluation of the revised analytical model based on the subassembly experiments. The analytical models use the results from the material tests shown in Table 2 and Fig. 3.

Coupling Shear Force versus Rotation Relationships

Fig. 10(a) shows the predicted coupling shear force versus rotation ($V_b - \theta_b$) relationships from Tests 1, 3, and 5. Comparisons with the measured relationships in Figs. 5 and 7 indicate that the revised model

provides a good representation of the global behavior of the test specimens. The increase in the coupling shear resistance and stiffness due to the kinking of the PT strands in Test 1 is captured. Note that this effect is not evident in the V_b - θ_b relationships of the other test specimens since the kinking of the PT strands occurs at large rotations (due to the use of oversized PT ducts) and the increase in stiffness due to kinking is counteracted by the reduction in stiffness due to deterioration in the top and seat angles. The failure of the test specimens (i.e., reduction in the coupling shear resistance) due to low cycle fatigue of the angles or due to fracture of the PT strands is not captured by the analytical model.

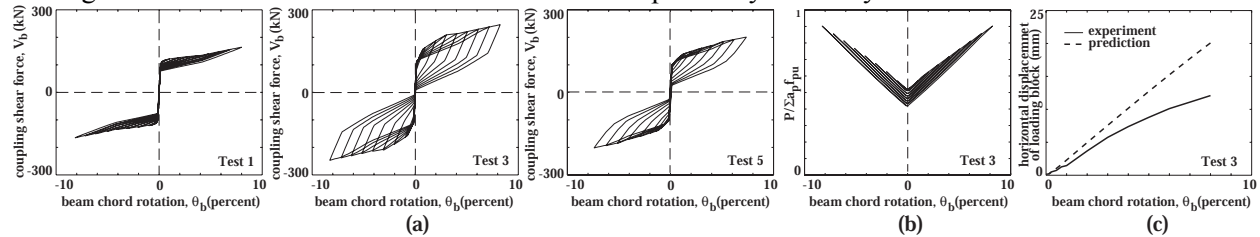


Fig. 10. Model verification: (a) V_b - θ_b relationships - Tests 1, 3, 5; (b) total PT force -Test 3; and (c) horizontal displacements - Test 3

Coupling Beam Post-Tensioning Forces

Fig. 10(b) shows the predicted results for the total PT force in Test 3, normalized with respect to the design ultimate strength of the strands, $\Sigma_a p f_{pu}$. Comparisons with the measured force in Fig. 6(c) indicate that the analytical model is capable of predicting not only the increase in the PT force due to increased displacements of the subassembly, but also the loss in the PT force (upon unloading to zero displacement) due to nonlinear behavior in the structure. The results in Fig. 10(b) show that the analytical model overestimates slightly the increase in the total PT force as the subassembly is displaced. In order to investigate this difference, Fig. 10(c) compares the measured and predicted displacements of the loading block in the horizontal direction as the beam is rotated. The positive displacements indicate that the loading block moves away from the reaction block. These horizontal displacements, which occur primarily due to the opening of gaps at the beam-to-wall interfaces, are directly related to the total elongations of the PT strands, and thus, the PT forces. The comparisons indicate that the analytical model overestimates the horizontal displacements of the loading block at large rotations, and thus overestimates the elongations of the PT tendons, resulting in the overestimated PT force in Fig. 10(b).

Behavior at Coupling Beam Ends

To evaluate the capability of the analytical model to predict the behavior at the coupling beam ends, Fig. 11(a) compares the measured and predicted results for the “average” compressive strains in the beam

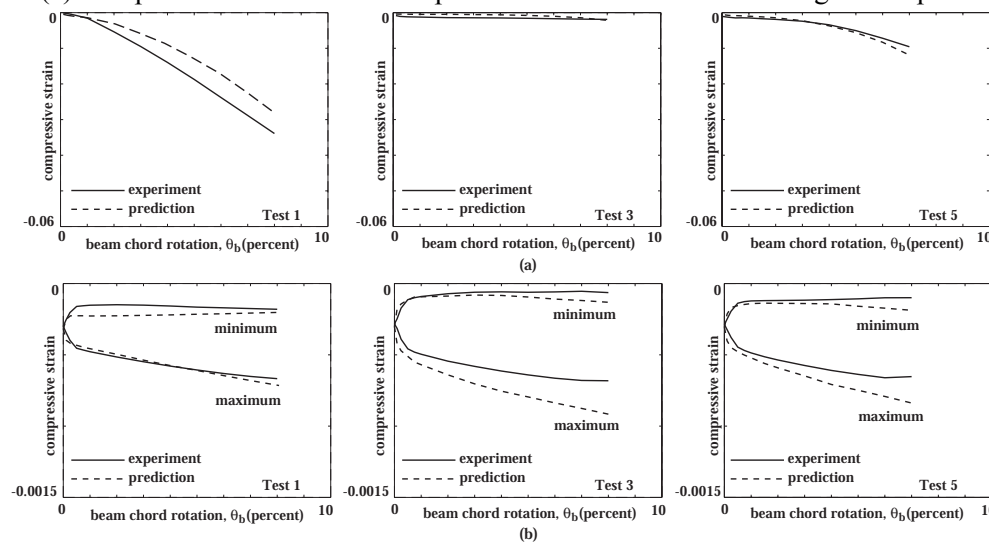


Fig. 11. Model verification - Tests 1, 3, 5: (a) beam cover plate/flange strains; and (b) beam web strains

contact regions from Tests 1, 3, and 5. Beam cover plate (for Test 1) and flange (for Tests 3 and 5) strain gages SG5-SG22 (Fig. 4) were used for this purpose. To calculate the measured average strains, first, the total compressive deformation from each set of strain gages was

calculated by assuming a linear strain distribution between the gages, extrapolated to the beam end. Then, the average strains were calculated by dividing the total deformation measured for each gage set with the distance from the last gage to the beam end. The predicted “average” strains for the same length of cover plate or flange were determined using the analytical model. No attempt was made to compare the strains measured at individual gage locations with the predicted values, since the measured strains varied considerably due to uneven contact at the beam ends. The comparisons in Fig. 11(a) indicate that, while there are discrepancies between the measured and predicted values, the analytical model is capable of providing a satisfactory representation of the local contact behavior at the ends of the coupling beams.

Behavior Along the Beam Span

In order to evaluate the capability of the analytical model to predict the behavior of the coupling beams along the span, Fig. 11(b) compares the measured and predicted “average” maximum/minimum compressive strain values in strain gages SG1-SG4 from Tests 1, 3, and 5. Note that when θ_b is positive (i.e., clockwise), maximum compression strains of similar value are measured in gages SG2 and SG3, and minimum compressive strains of similar value are measured in gages SG1 and SG4, since these gage pairs are symmetrically placed inside the diagonal compression field. As the beam is rotated in the negative direction, the maximum and minimum readings in the gage pairs alternate. The measured strains in Fig. 11(b) are calculated as the average maximum and minimum readings from all four gages. The results indicate that the analytical model provides reasonable estimates of the beam web strains along the span.

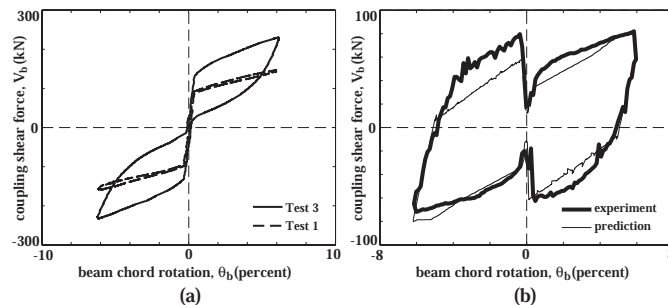


Fig. 12. Angle behavior: (a) Tests 1 and 3; and (b) cyclic behavior

Cyclic Behavior of Top and Seat Angles

As shown in Table 1, the only significant difference between Tests 1 and 3 is the use of four angles at the beam-to-wall interfaces. The contribution of these angles to the coupling shear force was determined by “subtracting” the V_b - θ_b relationship of Test 1 from that of Test 3 as shown in Fig. 12(a). The resulting V_b - θ_b relationship for a cycle of loading to $\theta_b = \pm 6\%$ is shown by the thick line in Fig. 12(b). The predicted difference between Tests 1 and 3 using the revised analytical model is shown by the thin line in Fig. 12(b). The comparisons between the predicted and measured results indicate that the proposed angle model provides a reasonable representation of the behavior of the top and seat angles under cyclic loading. Low cycle fatigue of the angles is not modeled.

Recommendations for Application

Based on the experiments described in this paper, the PT anchors and the angle-to-wall and angle-to-beam connections are the most critical components that can affect the performance of an unbonded post-tensioned hybrid coupling system. Anchor types other than the steel wedge/barrel system used in this research may improve the performance of the PT tendons. It may also be possible to grout a short length of the tendons near the anchors to prevent premature fracture of the strands inside the anchors. Kinking of the PT strands during the experiments did not have any adverse effects on the performance of the strands. The slip critical angle-to-beam connections used in the test specimens worked well. The post-tensioned angle-to-wall connections also performed well, with no yielding in the connection strands and no damage in the concrete. The beam-to-wall connections should be designed to transfer the maximum coupling shear forces without slip. The experimental results showed that the use of beam flange cover plates is not necessary for beam nominal initial stress, f_{bi} values (see Table 1) up to 25% of the steel yield strength, as long as compact sections are used for the beams. The use of confinement reinforcement inside the concrete and steel plates at the beam-to-wall interfaces is necessary to prevent damage in the wall concrete. The shim plates used in the experiments ensured contact between the walls and the beam flanges throughout the displacement history, and thus, their use in practice is recommended.

A design approach to ensure the desirable behavior of the proposed coupling system based on the results of this experimental program is described in Shen et al. [4], [10].

SUMMARY AND CONCLUSIONS

This paper describes an experimental program on the nonlinear behavior of unbonded post-tensioned hybrid coupled wall subassemblages. The test results demonstrate that the proposed system has excellent stiffness, strength, and ductility under cyclic loading. The nonlinear deformations of a properly designed subassemblage occur primarily due to the opening of gaps at the beam-to-wall interfaces. As a result of post-tensioning, the initial stiffness of the subassemblage is similar to the initial stiffness of a subassemblage with embedded steel beams. The post-tensioning force provides a restoring force that closes the gaps and pulls the walls and the beams back towards their undisplaced position upon unloading from a large nonlinear deformation, resulting in a self-centering capability. The subassemblages can be designed to provide significant and stable levels of coupling with most of the damage occurring in top and seat angles at the beam ends, which can be replaced after an earthquake. It is concluded that unbonded post-tensioned steel beams provide an effective and feasible means to couple reinforced concrete walls. Comparisons with the experimental results indicate that the proposed analytical model provides a good representation of not only the global behavior, but also the local behavior of the subassemblages.

ACKNOWLEDGEMENTS

The investigation was funded by the National Science Foundation (NSF) under Grant No. CMS 98-10067 as a part of the *U.S.-Japan Cooperative Earthquake Research Program on Composite and Hybrid Structures*. The support of the NSF Program Director Dr. S. C. Liu and Coordinators Drs. S. Goel and S. Mahin is gratefully acknowledged. The opinions, findings, and conclusions are those of the authors and do not necessarily reflect the views of the NSF or the individuals and organizations acknowledged above.

REFERENCES

1. Harries, K., Gong, B., and Shahrooz, B. "Behavior and design of reinforced concrete, steel, and steel-concrete coupling beams." *Earthquake Spectra*, 16(4), 2000, 775-799.
2. Shen, Q., and Kurama, Y. "Nonlinear behavior of posttensioned hybrid coupled wall subassemblages." *J. Struct. Eng.*, 128(10), 2002, 1290-1300.
3. Kurama, Y. and Shen, Q. "Posttensioned hybrid coupled walls under lateral loads." *J. Struct. Eng.*, 130(2), 2004, 297-309.
4. Shen, Q., Kurama, Y., and Weldon, B. "Seismic analysis, behavior, and design of unbonded post-tensioned hybrid coupled walls." *Structural Engineering Research Report #NDSE-04-01*, Dept. of Civil Eng. and Geol. Sci., Univ. of Notre Dame, Notre Dame, Indiana, expected 2004.
5. Kurama, Y., Weldon, B., and Shen, Q. "Experimental evaluation of post-tensioned hybrid coupled wall subassemblages." *J. Struct. Eng.*, submitted 2003.
6. AISC. "Manual of steel construction load and resistance factor design." American Institute of Steel Construction, Third Edition, 2001.
7. Prakash, V., Powell, G., and Campbell, S. "DRAIN-2DX base program description and user guide; Version 1.10." *Rep. UCB/SEMM-93/17*, Dept. of Civil Eng., Univ. of California, Berkeley, 1993.
8. Kishi, N. and Chen, W. "Moment-rotation relations of semirigid connections with angles." *J. Struct. Eng.*, 116(7), 1990, 1813-1834.
9. Lorenz, R., Kato, B., and Chen, W. "Semi-rigid connections in steel frames." Council on Tall Buildings and Urban Habitat, Committee 43, McGraw-Hill, Inc., 1993.
10. Shen, Q., Kurama, Y., and Weldon, B. "Analytical modeling and design of post-tensioned hybrid coupled wall subassemblages." *J. Struct. Eng.*, submitted 2003.